

A Co_3O_4 Cage/ MnO_2 Nanosheet Composite: An Enhanced Electrode Material for Flexible All-Solid-State Supercapacitors

Xu Zhang,* Heng Xiang, Chuang Pang, Keyu Zhao, Zhongli Zou, and Kui Cheng

The development of flexible energy-storage devices is limited by the poor conductivity, limited cycling stability, and slow electron/ion transport of metal oxides. Optimizing their structure and performance is crucial for advancing these technologies. Herein, a hollow cubic core–shell $\text{Co}_3\text{O}_4@\text{MnO}_2$ is synthesized via annealing and hydrothermal approaches. This composite enjoys advantages of the high electrical conductivity of Co_3O_4 and the excellent pseudocapacitive properties of MnO_2 ; in addition, the hollow structure of the composite effectively mitigates the mechanical stress caused by volume changes during charge–discharge cycles. Owing to its large specific surface area and stable framework, $\text{Co}_3\text{O}_4@\text{MnO}_2$ achieves a high specific capacitance of 670.2 F g^{-1}

and retains 83.18% of its initial capacitance after 10,000 cycles, demonstrating exceptional electrochemical stability and durability. Subsequently, an all-solid-state flexible supercapacitor was assembled using $\text{Co}_3\text{O}_4@\text{MnO}_2$ positive electrode and a negative electrode made of reduced graphene oxide hydrogel. The device achieves a high energy density of 78.2 W h kg^{-1} and a power density of $11,500 \text{ W kg}^{-1}$. Further, even after 10,000 charge–discharge cycles, it retained 73.1% of its initial capacitance, demonstrating potential for flexible energy-storage applications. This article highlights the advantages of $\text{Co}_3\text{O}_4@\text{MnO}_2$ in enhancing supercapacitor performance and offers insights for cost-effective cobalt-based energy-storage systems.

1. Introduction

Owing to the increasing energy crisis and environmental pollution, developing efficient high-power-density energy-storage devices has become critical. Supercapacitors, which have excellent power densities, long lifespans, and rapid charge–discharge characteristics, have found widespread applications in electric vehicles, renewable energy storage, and smart grids, bridging the gap between traditional capacitors and batteries.^[1] However, the performance of supercapacitors is often constrained by the selection of electrode material and their microstructural design. Ideal electrode materials should have high specific surface areas, good electrical conductivities, excellent chemical stabilities, and uniformly distributed pore structures. Transition-metal oxides, including Fe_xO_y ,^[2] Cu_xO_y ,^[3] Co_3O_4 ,^[4] Mn_xO_y ,^[5] and NiO ,^[6] have attracted considerable research attention owing to their high theoretical specific capacities and significant pseudocapacitive properties. Despite their high theoretical

capacities, the practical applications of these materials are limited by poor electrical conductivities and suboptimal cycling stabilities, especially in high-power-demand scenarios.^[7] Moreover, the practical specific capacities of single-transition-metal oxides are often lower than their corresponding theoretical values. Consequently, these materials are frequently combined with carbon materials or other transition-metal oxides, and their microstructures are optimized to enhance overall performance. For example, manganese (Mn) is an abundant and inexpensive metal. Although MnO_2 is used as a pseudocapacitive material, it has a relatively low theoretical capacity, poor conductivity, and limited cycling performance.^[8] On the contrary, Co_3O_4 offers excellent conductivity, cycling stability, and a high theoretical capacity, but its high cost limits its widespread application.^[9] Therefore, combining these two materials via structural and compositional adjustments can yield a composite material at low cost, while achieving superior electrochemical performance. For instance, Xia et al. proposed a $\text{Co}_3\text{O}_4@\text{Pt}@{\text{MnO}_2}$ composite material, composed of Co_3O_4 nanowire arrays as the core and an ultra-thin shell of Pt nanoparticles and MnO_2 nanosheets covering the surface. This material had a charge storage capacity of 497 F g^{-1} , far exceeding the theoretical capacities of the individual metals, and showed enhanced cycling stability.^[10] However, capacity decay was observed by varying the current density. In another study, Wei et al. uniformly wrapped Co_3O_4 and MnO_2 onto super-aligned electrospun carbon nanofibers and tested them in 6 M KOH. They achieved a maximum energy density of 64.5 Wh kg^{-1} and maintained 71.8% of their capacity after 11,000 cycles. However, the maximum power density was only 3828 W kg^{-1} .^[11] These studies highlight the importance of rational electrode

X. Zhang, H. Xiang, C. Pang, K. Zhao, Z. Zou

School of Materials Science and Engineering, and Ningxia Research Center of Silicon Target and Silicon-Carbon Negative Materials Engineering Technology

North Minzu University
Yinchuan 750021, China
E-mail: zhangxu1024@nmu.edu.cn

K. Cheng
College of Engineering
Northeast Agricultural University
Harbin 150030, China

 Supporting information for this article is available on the WWW under <https://doi.org/10.1002/batt.202500291>

material design for enhancing overall supercapacitor performance.

In this study, a $\text{Co}_3\text{O}_4@\text{MnO}_2$ composite with a core–shell structure was designed. Here, Co_3O_4 nanocages form the core and MnO_2 nanosheets serve as the shell. This structural design exploits the synergistic effects of the two materials. Briefly, the core–shell configuration minimizes mechanical stress from volume changes during repeated charge–discharge cycles. Additionally, the hollow nanocage and nanosheet structures increase the number of active sites, enabling rapid charge and discharge, even at high current densities. From an energy storage perspective, combining Co_3O_4 and MnO_2 enhances the range of possible electrochemical reactions, and their interaction significantly improves the capacitance, exceeding the sum of the individual components alone. In conclusion, the proposed core–shell electrode design provides a novel strategy for developing high-performance materials for supercapacitors.

2. Experimental Section

All reagents were purchased from Shanghai Aladdin Biochemical Technology (Shanghai, China). All reagents were of analytical grade and used directly after purchase without any further purification.

2.1. Material Preparation

2.1.1. Preparation of $\text{Co}_3[\text{Co}(\text{CN})_6]_2$

CoCl_2 (0.6 mmol) and $\text{C}_6\text{H}_5\text{Na}_3\text{O}_7$ (0.9 mmol) were dissolved in deionized water (40 mL), and $\text{K}_3[\text{Co}(\text{CN})_6]$ (0.4 mmol) was added. The mixture was stirred for 10 min and incubated at room temperature for 24 h. The precipitate was washed with distilled water and ethanol and then dried at 60 °C for 12 h to obtain $\text{Co}_3[\text{Co}(\text{CN})_6]_2$.

2.1.2. Preparation of Co_3O_4

The prepared $\text{Co}_3[\text{Co}(\text{CN})_6]_2$ powder was heated in air at a rate of 2 °C min⁻¹ to 350 °C and held for 2 h. It was then cooled to room temperature to obtain Co_3O_4 powder.

2.1.3. Preparation of $\text{Co}_3\text{O}_4@\text{MnO}_2$

Co_3O_4 (0.05 mmol) and KMnO_4 (0.05 mmol) were dispersed in distilled water (40 mL) and transferred into an autoclave. The reaction was carried out at 150 °C for 2 h. After cooling to room temperature, the resulting $\text{Co}_3\text{O}_4@\text{MnO}_2$ was washed with distilled water and ethanol by centrifugation and then dried at 60 °C.

2.1.4. Preparation of rGOH

Graphene oxide (GO) was prepared using Hummer's method,^[12] that is, graphite was oxidized with concentrated H_2SO_4 and

KMnO_4 at controlled temperatures (0–35 °C). The oxidation reaction was terminated by adding H_2O_2 , and the resulting product was thoroughly washed with deionized water and dilute HCl to remove impurities. The washed GO was then exfoliated and dried. For hydrogel preparation, GO powder (0.3 g) was dispersed in deionized water (70 mL), and NaHSO_3 solution (10 mL, 0.5 mmol L⁻¹) was added. The mixture was transferred to a 100 mL autoclave and subjected to hydrothermal treatment at 180 °C for 8 h, yielding rGOH.

2.2. Assembly of $\text{Co}_3\text{O}_4@\text{MnO}_2||\text{rGOH}$

The Co_3O_4 and $\text{Co}_3\text{O}_4@\text{MnO}_2$ electrodes were fabricated by coating a slurry onto a nickel foam substrate. The slurry was prepared by dispersing the active material, acetylene black, and polytetrafluoroethylene (PTFE) in ethanol at a mass ratio of 75:20:5. The rGOH electrode was obtained by slicing the columnar reduced graphene oxide (rGO) synthesized via a hydrothermal reaction and then pressing the slices onto the nickel foam substrate under a pressure of 1 MPa. An asymmetric flexible all-solid-state supercapacitor was assembled by matching its capacitance with that of the rGOH electrode, based on Equation (1).^[13]

$$m^+/m^- = C^-V^-/C^+V^+ \quad (1)$$

Here, C^-/C^+ and V^-/V^+ represent the capacitance and voltage range ratios of the negative and positive electrodes, respectively.

The assembly process of $\text{Co}_3\text{O}_4@\text{MnO}_2||\text{rGOH}$ was as follows: Polyvinyl alcohol (PVA, 1 g) was soaked in Na_2SO_4 electrolyte (10 mL, 0.5 mol L⁻¹) for 12 h. The mixture was then heated to 80 °C and stirred until clear. After cooling, a Na_2SO_4 -PVA gel electrolyte was formed. The gel was applied to a filter paper, and the positive and negative electrodes were sandwiched on either side. Solidification occurred at room temperature. The assembly of $\text{Co}_3\text{O}_4@\text{MnO}_2||\text{rGOH}$ was then completed, and the device was prepared for testing.

2.3. Characterization

The chemical compositions of all samples were analyzed by X-ray diffractometry (XRD, XRD-6000, Shimadzu, Kyoto, Japan) and X-ray photoelectron spectroscopy (XPS) (ESCALAB 250Xi, Thermo Fisher Scientific, Waltham, MA, USA). The morphology and structural features were investigated by field-emission scanning electron microscopy (SEM; Supra 55, Zeiss, Oberkochen, Germany) and transmission electron microscopy (TEM; FEI Tecnai F20, Thermo Fisher Scientific). The porosity and specific surface area were measured using a Quantachrome Instruments Autosorb iQ2 gas sorption analyzer (Anton Paar, Graz, Austria) under low pressure (0–1.0 bar). Before analysis, samples were evacuated under high vacuum at 120 °C for 10 h to ensure purity and stability.

2.4. Electrochemical Measurements

For the measurements, an Ag/AgCl electrode served as the reference electrode, whereas a graphite rod functioned as the

counter electrode. Cyclic voltammetry (CV), galvanostatic charge-discharge (GCD), and electrochemical impedance spectroscopy (EIS) analyses were performed on all samples using an electrochemical workstation (CS2350M, CORRTEST, Wuhan, China) at room temperature, controlled using CS Studio. To evaluate cycle stability, a battery testing system (CT3002A, Wuhan LAND Electronic, Wuhan, China) was employed.

The gravitational specific capacitance (C_g) was determined from the discharge curves using Equation (2).^[14]

$$C_g = 2j \int V(t)dt / \Delta V^2 \quad (2)$$

The energy density (E , W h kg⁻¹) and power density (P , W kg⁻¹) for $\text{Co}_3\text{O}_4@\text{MnO}_2||\text{rGOH}$ were calculated using Equation (3) and (4).^[15]

$$E = C_g \Delta V^2 / 7.2 \quad (3)$$

$$P = 3600E / \Delta t \quad (4)$$

In these equations, j , ΔV , and Δt represent the current density (A g⁻¹) and discharge voltage (V), respectively.

3. Results and Discussion

To investigate the synthesis of $\text{Co}_3\text{O}_4@\text{MnO}_2$, XRD analysis was conducted on both Co_3O_4 and $\text{Co}_3\text{O}_4@\text{MnO}_2$ (Figure 1a). In the XRD pattern of Co_3O_4 , distinct reflections at 31.27°, 36.85°, and 59.35°, corresponding to the (220), (311), and (511) planes, respectively, of standard Co_3O_4 (JCPDS No. 43-1003) were observed.^[16] Similarly, the XRD pattern of MnO_2 contained reflections at 21.06°, 36.57°, and 65.08°, corresponding to the (101), (210), and (020) crystal planes, respectively (JCPDS No. 42-1316).^[17] Furthermore, no significant impurity peaks were observed in the XRD pattern of the composite material, confirming the synthesis of pure $\text{Co}_3\text{O}_4@\text{MnO}_2$.

Figure 1b shows the adsorption-desorption isotherms of Co_3O_4 and $\text{Co}_3\text{O}_4@\text{MnO}_2$, both of which exhibit distinct type-IV characteristics, indicating the presence of mesoporous structures.^[18] Notably, the adsorption capacity of $\text{Co}_3\text{O}_4@\text{MnO}_2$ was significantly higher than that of Co_3O_4 , indicating that the introduction of MnO_2 increased the specific surface area and improved the pore structure, thereby enhancing adsorption. As shown in Figure 1c, $\text{Co}_3\text{O}_4@\text{MnO}_2$ produced a distinct peak at 2–10 nm, indicating a high density of small mesopores. This optimized pore structure facilitates better contact between the

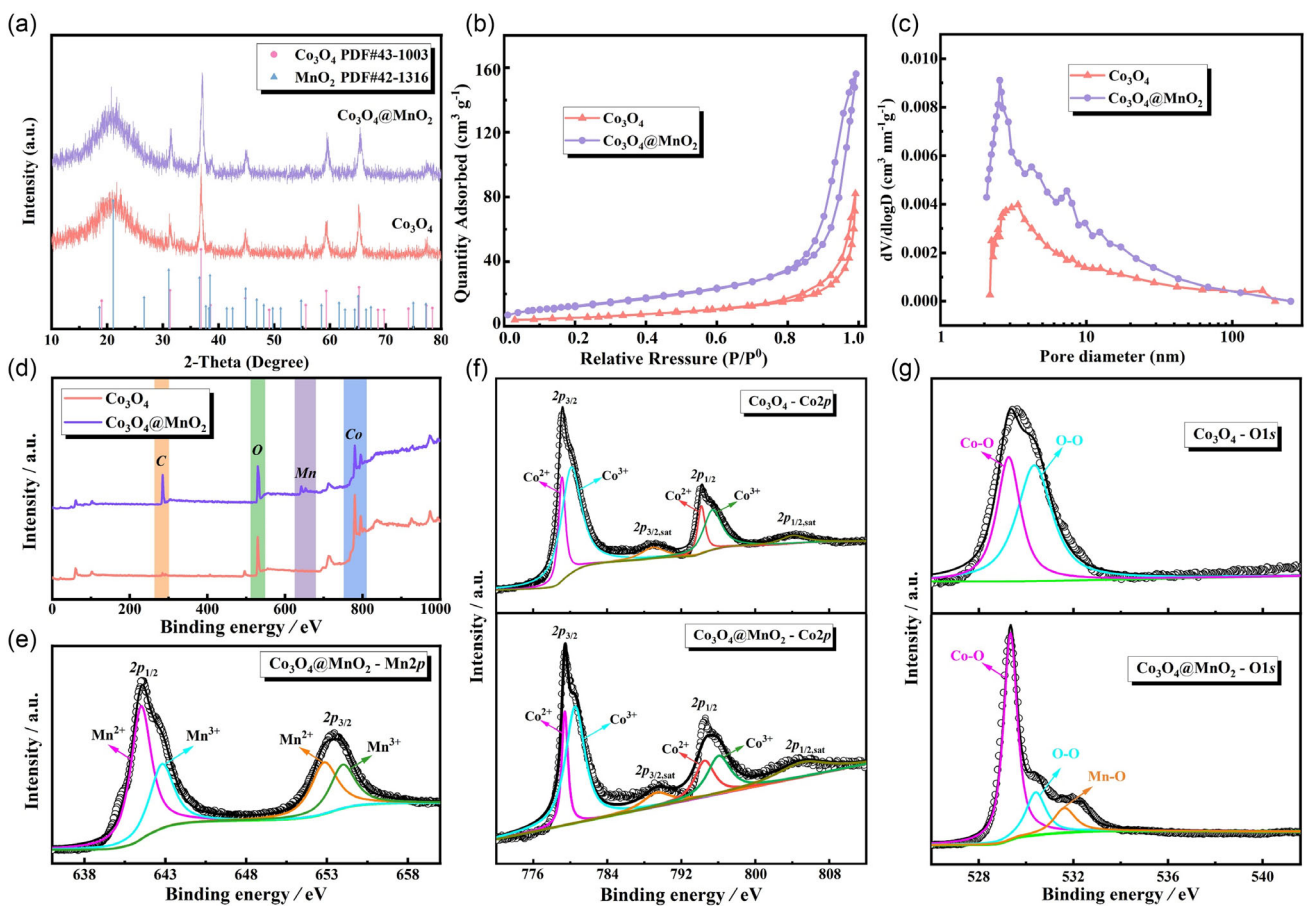


Figure 1. a) XRD patterns, b) N_2 adsorption–desorption isotherms, c) pore size distribution, and d) XPS wide-scan survey spectra. High-resolution e) Mn 2p, f) Co 2p, and g) O 1s XPS spectra.

electrolyte and electrode, providing a highway for ion transport and substantially enhancing the electrochemical performance of the active materials.

The elemental compositions and valence states of Co_3O_4 and $\text{Co}_3\text{O}_4@\text{MnO}_2$ were further investigated using XPS. As shown in Figure 1d, the full-spectrum XPS profiles of Co_3O_4 and $\text{Co}_3\text{O}_4@\text{MnO}_2$ confirm the integration of Mn with no impurities. Figure 1e presents the high-resolution Mn 2p XPS profile of $\text{Co}_3\text{O}_4@\text{MnO}_2$. The Mn 2p peak was deconvoluted into Mn 2p_{3/2} and Mn 2p_{1/2} spin-orbit doublets at binding energies of 642.39 and 653.82 eV, respectively. Further deconvolution revealed characteristic peaks corresponding to Mn²⁺ at 642.0 and 653.1 eV, and Mn³⁺ at 643.0 and 654.2 eV, confirming the presence of these species.^[19] Figure 1f shows the high-resolution Co 2p XPS profiles of Co_3O_4 and $\text{Co}_3\text{O}_4@\text{MnO}_2$, showing similar valence states in both. The Co 2p_{3/2} and Co 2p_{1/2} main peaks were observed at 781.7 and 799.39 eV, with satellite peaks at 786.37 and 796.9 eV, confirming the presence of mixed-valence cobalt ions.^[20] The high-resolution O 1s profile of Co_3O_4 (Figure 1g) was deconvoluted into two components, corresponding to Co—O and O—O bonds at 529.8 and 530.8 eV, respectively. In contrast, the O 1s spectrum of $\text{Co}_3\text{O}_4@\text{MnO}_2$ contained a peak corresponding to Mn—O bonds at 531.6 eV, confirming the growth of the MnO_2 shell. Thus, the XPS analysis revealed the presence of mixed-valence states of Co (Co²⁺ and Co³⁺), which should facilitate charge transfer. Further, the introduction of mixed-valence states of Mn should enhance ion and electron transport, improving charge storage efficiency, giving $\text{Co}_3\text{O}_4@\text{MnO}_2$ excellent pseudocapacitive characteristics, and synergistically optimizing the capacitive performance of $\text{Co}_3\text{O}_4@\text{MnO}_2$.

Figure 2a shows the evolution of the microstructure during the synthesis of the $\text{Co}_3\text{O}_4@\text{MnO}_2$ composites, as analyzed using SEM. Initially, $\text{Co}_3[\text{Co}(\text{CN})_6]_2$ nanocubes were prepared using a simple room-temperature aging process. The SEM images (Figure 2b,c) indicate that the resulting $\text{Co}_3[\text{Co}(\text{CN})_6]_2$ nanocubes have smooth and flat surfaces and sizes predominantly distributed around 600 nm. Subsequently, the $\text{Co}_3[\text{Co}(\text{CN})_6]_2$ nanocubes were converted into Co_3O_4 nanocages via calcination. As shown in the SEM images (Figure 2d,e), the Co_3O_4 nanocages comprise numerous granular subunits and have a rough surface morphology. Finally, $\text{Co}_3\text{O}_4@\text{MnO}_2$ composites were synthesized via hydrothermal growth of MnO_2 on the surface of Co_3O_4 nanocages. The SEM images (Figures 2f,g) reveal that the composites retained the overall morphology of the Co_3O_4 nanocages, but their surfaces were uniformly coated with MnO_2 nanosheets. TEM analysis (Figures 2h,i) further confirmed that the MnO_2 nanosheet layers grew evenly on the surface of the Co_3O_4 nanocages. In the MnO_2 layers (Figure 2j), lattice spacings of 0.189 and 0.241 nm are observed, corresponding to the (200) and (211) planes of MnO_2 , respectively. In the Co_3O_4 layers (Figure 2k), lattice spacings of 0.464 and 0.244 nm were observed, corresponding to the (311) and (111) planes of Co_3O_4 , respectively. Additionally, the selected-area electron diffraction (SAED) pattern of the $\text{Co}_3\text{O}_4@\text{MnO}_2$ composite (Figure 2l) reveals distinct diffraction rings, indicating a highly ordered crystalline lattice. Calculations based on Bragg's law identified the (200), (211),

and (411) planes of MnO_2 , as well as the (220), (400), and (440) planes of Co_3O_4 , further validating the polycrystalline nature of Co_3O_4 and MnO_2 and their co-presence within the composites. These lattices spacing measurements are in good agreement with the XRD results. In addition, the energy-dispersive X-ray spectroscopy (EDS) element maps (Figure 2m) reveal the uniform distribution of Mn, Co, and O within the composites. Collectively, these results confirm the synthesis of $\text{Co}_3\text{O}_4@\text{MnO}_2$ composites with well-defined hollow structures, homogeneous elemental distributions, and excellent crystalline characteristics, providing a robust structural foundation for electrochemical applications.

To investigate the electrochemical performance of $\text{Co}_3\text{O}_4@\text{MnO}_2$, CV, GCD measurements, and EIS were performed using a three-electrode system with 6 M KOH as the electrolyte. As shown in Figure 3a, the CV curves of Co_3O_4 and $\text{Co}_3\text{O}_4@\text{MnO}_2$ at a scan rate of 40 mV s⁻¹ reveal typical pseudocapacitive behavior. Notably, the CV curve of $\text{Co}_3\text{O}_4@\text{MnO}_2$ encloses a larger area, indicating its superior charge storage capacity. Figure 3b shows the CV curves of $\text{Co}_3\text{O}_4@\text{MnO}_2$ at scan rates ranging from 5 to 80 mV s⁻¹. As the scan rates increased, the peak currents increased significantly, but the CV curve shapes remained consistent, indicating high reversibility.

As shown in Figure 3c, both the anodic and cathodic peak current densities (I_p) for Co_3O_4 and $\text{Co}_3\text{O}_4@\text{MnO}_2$ show a perfect linear relationship with the square root of the scan rate (v). Based on the Randles–Sevcik equation, the apparent diffusion coefficient (D) for OH⁻ can be expressed as follows.^[21]

$$D = I_p^2 / (2.69 \times 10^5 \times n^{1.5} \times A \times C \times v^{0.5})^2 \quad (5)$$

Here, n , A , and C are the number of electrons, electrode surface area, and proton concentration, respectively. A comparison of the apparent diffusion coefficients of Co_3O_4 and $\text{Co}_3\text{O}_4@\text{MnO}_2$ at specific scan rates revealed that $\text{Co}_3\text{O}_4@\text{MnO}_2$ exhibited greater ion mobility, highlighting its superior ion-diffusion characteristics.

Figure 3d presents the GCD curves of Co_3O_4 and $\text{Co}_3\text{O}_4@\text{MnO}_2$ at a current density of 1 A g⁻¹. The discharge time of $\text{Co}_3\text{O}_4@\text{MnO}_2$ was significantly longer than that of Co_3O_4 , reflecting an 81% performance enhancement. The electrochemical performance of Co_3O_4 is shown in Figure S1, Supporting Information. Analysis of the GCD curves at various current densities (Figure 3e) revealed that the voltage plateaus correspond to the redox peaks in the CV curves, whereas the nearly symmetrical charge and discharge times indicate the excellent reversibility and outstanding charge storage capability of $\text{Co}_3\text{O}_4@\text{MnO}_2$. Using (Equation 2), the specific capacitance of $\text{Co}_3\text{O}_4@\text{MnO}_2$ was found to be 670.2 F g⁻¹ at 1 A g⁻¹ (367.5 F g⁻¹ for Co_3O_4). Furthermore, even at a high current density of 30 A g⁻¹, $\text{Co}_3\text{O}_4@\text{MnO}_2$ retained 88.07% of its initial capacitance. This exceptional rate capability can be attributed to the unique hollow core–shell structure, which enhances the ion-diffusion paths and facilitates rapid redox reactions. The electrochemical performance of core–shell structured materials in recent years is summarized in Table S1, Supporting Information, highlighting the superior charge-storage capabilities of $\text{Co}_3\text{O}_4@\text{MnO}_2$.

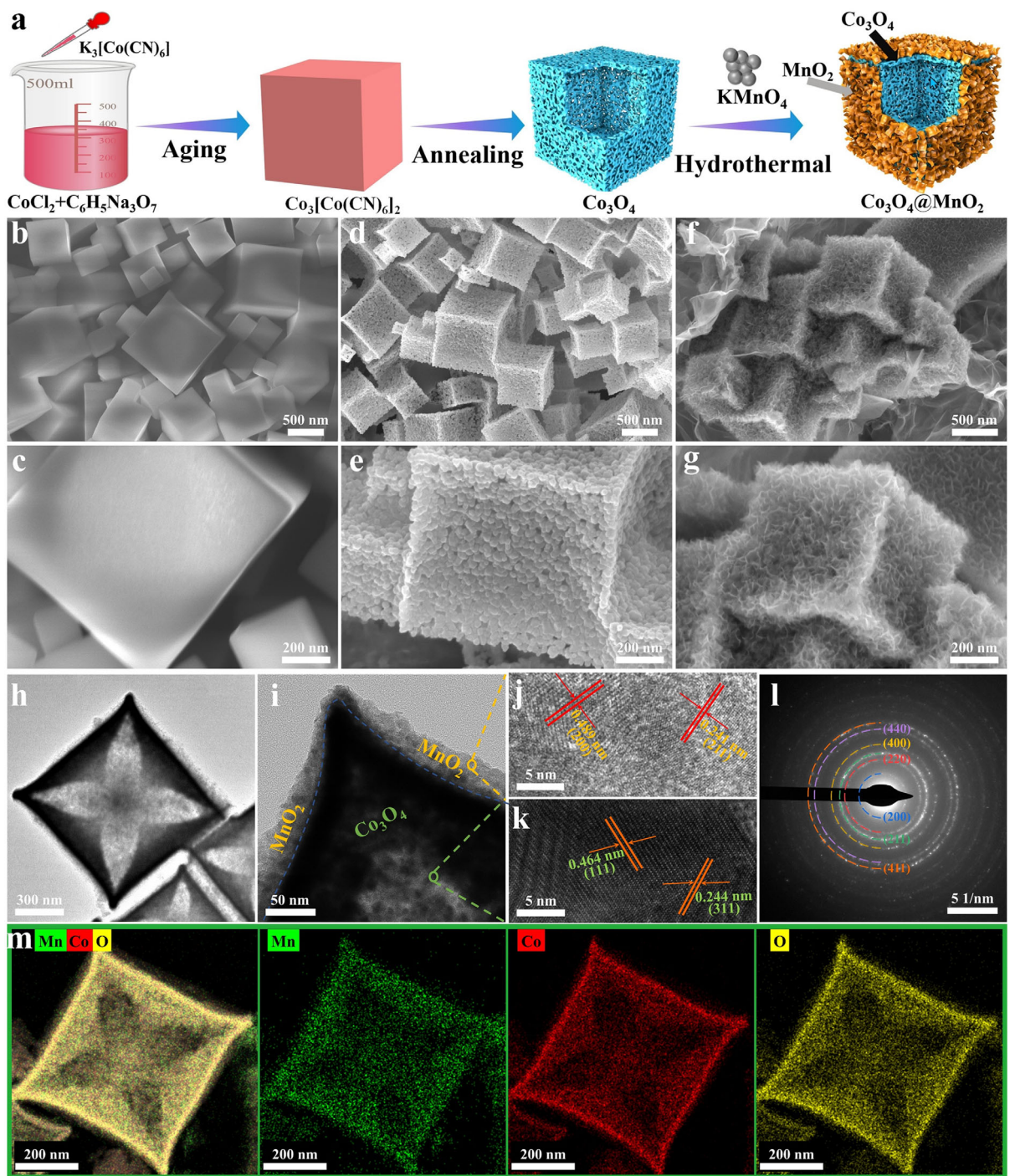


Figure 2. a) Schematic diagram of the synthesis process for $\text{Co}_3\text{O}_4 @ \text{MnO}_2$; SEM images of b,c) $\text{Co}_3[\text{Co}(\text{CN})_6]_2$, d,e) Co_3O_4 , and f,g) $\text{Co}_3\text{O}_4 @ \text{MnO}_2$. h,i) TEM, j,k) high-resolution TEM, and l) selected-area electron diffraction patterns of $\text{Co}_3\text{O}_4 @ \text{MnO}_2$. m) EDS maps of Mn, Co, and O.

Figure 3g displays the EIS results for both materials. The equivalent series resistance (R_s), determined from the intercept of the curves on the real axis, is 1.57Ω for Co_3O_4 and 1.39Ω for $\text{Co}_3\text{O}_4 @ \text{MnO}_2$, suggesting that the hollow cubic core–shell structure of $\text{Co}_3\text{O}_4 @ \text{MnO}_2$ significantly improves electron transport and reduces resistance. At intermediate frequencies, the semicircular diameter represents the double-layer capacitance and charge-transfer resistance (R_{ct}) at the electrolyte/electrode

interface. Thus, $\text{Co}_3\text{O}_4 @ \text{MnO}_2$ showed superior electronic conductivity and interfacial charge-transfer capabilities.^[22] At low frequencies, the greater slope of the $\text{Co}_3\text{O}_4 @ \text{MnO}_2$ curve indicates lower ion-diffusion resistance and enhanced electron transport efficiency, further confirming its excellent pseudocapacitive behavior.^[21a,23] Detailed electrochemical parameters, derived from equivalent circuit fitting (see Figure S2 and Table S2, Supporting Information), further support these observations.

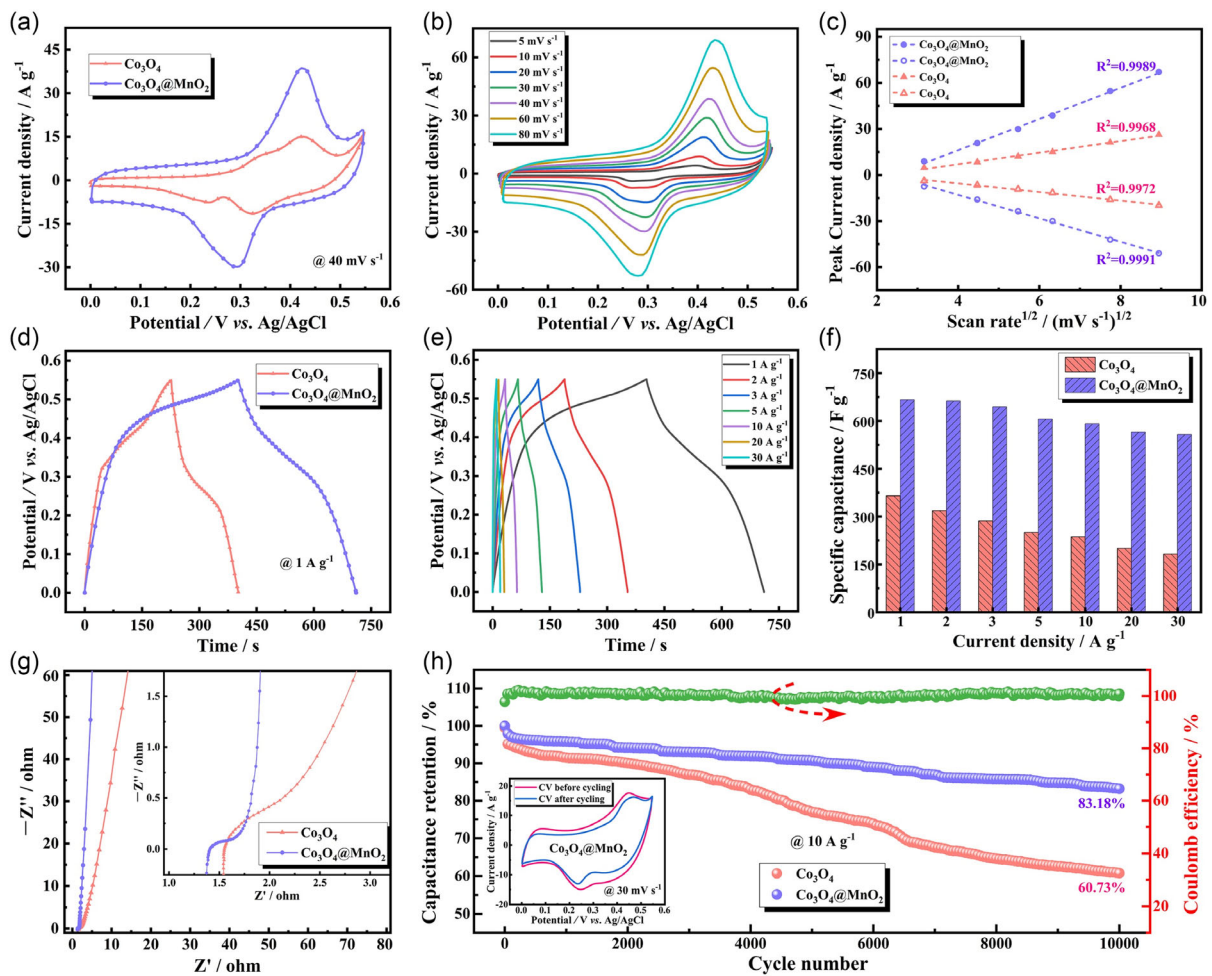


Figure 3. a) CV curves at a scan rate of 40 mV s^{-1} . b) CV curves of $\text{Co}_3\text{O}_4@\text{MnO}_2$ at different scan rates. c) Peak current density versus square root of scan rate and d) GCD curves at a current density of 1 A g^{-1} of Co_3O_4 and $\text{Co}_3\text{O}_4@\text{MnO}_2$. e) GCD curves of $\text{Co}_3\text{O}_4@\text{MnO}_2$ at different current densities. f) Specific capacitance against current density, g) Nyquist plots, and h) the capacitance retention and coulombic efficiency of Co_3O_4 and $\text{Co}_3\text{O}_4@\text{MnO}_2$. Inset compares the CV curves of $\text{Co}_3\text{O}_4@\text{MnO}_2$ before and after cycling.

Figure 3h compares the cycling stability of the two electrodes at a current density of 10 A g^{-1} . As shown, $\text{Co}_3\text{O}_4@\text{MnO}_2$ retains 83.18% of its initial capacitance after 10,000 cycles, significantly outperforming Co_3O_4 . Additionally, $\text{Co}_3\text{O}_4@\text{MnO}_2$ achieved nearly 100% coulombic efficiency, further demonstrating its outstanding charge-discharge reversibility. Post-cycling SEM analysis (Figure S3, Supporting Information) reveals that while minor detachment of MnO_2 nanosheets occurred during prolonged cycling, the core-shell architecture of $\text{Co}_3\text{O}_4@\text{MnO}_2$ remains largely intact. During cycling, the MnO_2 shell not only contributes to capacitance but also helps stabilize the structure of the Co_3O_4 nanocages, effectively mitigating structural collapse in the composite material. Furthermore, XPS analysis (Figure S4, Supporting Information) revealed the valence evolution of Co and Mn in the post-cycled electrode materials. As shown in Table S3, Supporting Information, the content of Co^{2+} and Mn^{2+} species increased significantly after multiple charge/discharge cycles, while the proportion of their +3 valence states decreased correspondingly. This indicates the occurrence of irreversible redox reactions during cycling, which directly contributed to the degradation of

charge storage performance. These findings highlight the exceptional long-term stability, high energy-storage efficiency, and superior rate performance of $\text{Co}_3\text{O}_4@\text{MnO}_2$. These characteristics make it particularly suitable for energy-storage devices requiring frequent charge-discharge operations, demonstrating its potential for widespread application in electrochemical energy storage.

The exceptional electrochemical performance of $\text{Co}_3\text{O}_4@\text{MnO}_2$ can be attributed to several factors. First, its unique core-shell structure significantly increases the specific surface area of the material, providing abundant active sites that facilitate electrochemical reactions and enhance redox kinetics, thereby improving overall energy-storage capacity. Second, the MnO_2 incorporation serves dual functions: it not only optimizes electron transport pathways, reduces internal resistance, and minimizes ion-diffusion resistance, but also alleviates the volume variation of Co_3O_4 nanocages during cycling, thereby enhancing structural stability. These synergistic effects collectively boost electron transfer kinetics, accelerate electrochemical reactions, and ultimately yield superior electrochemical performance with remarkable cycling durability. Furthermore, the presence of Co and Mn with multiple valence

states in the composite material plays a vital role in redox reactions, contributing to greater energy-storage capabilities and further boosting performance. The integration of these structural and material advantages endows $\text{Co}_3\text{O}_4@\text{MnO}_2$ with remarkable electrochemical properties, highlighting its potential for use in electrochemical energy storage.

To evaluate the practical applications of $\text{Co}_3\text{O}_4@\text{MnO}_2$ comprehensively, rGOH was used as the negative electrode and Na_2SO_4 -PVA was used as the solid-state electrolyte to assemble an all-solid-state energy-storage device, denoted $\text{Co}_3\text{O}_4@\text{MnO}_2||\text{rGOH}$ (Figure 4a). The electrochemical characteristics of rGOH are detailed in Figure S5, Supporting Information. The CV curves of rGOH and $\text{Co}_3\text{O}_4@\text{MnO}_2$ at a scan rate of 20 mV s^{-1} are shown in Figure 4b. The working voltage ranges for the positive and negative electrodes ranged from 0 to 0.6 V and from -1 to 0 V, respectively. Based on these ranges, the theoretical voltage window of the device was determined to be 0–1.6 V. The loading of the active materials in the device was determined using (Equation 1),

Figure 4c shows the CV curves of the device at different scan rates within the voltage range of 0–1.6 V. The consistent shape of the curves at various scan rates indicates the excellent rate performance of the device.

Based on the GCD curves of the $\text{Co}_3\text{O}_4@\text{MnO}_2/\text{rGOH}$ at different current densities (Figure S6, Supporting Information), the energy and power densities calculated using (Equation 3) and (4), respectively, are shown in Figure 4d. The device exhibited a power density of $11,500 \text{ W kg}^{-1}$ at an energy density of 52.2 W h kg^{-1} and achieved a maximum energy density of 78.2 W h kg^{-1} at a power density of 325 W kg^{-1} . These results demonstrate that the performance is significantly superior to previously reported Co_3O_4 -based and related composite materials (Table 1).^[24–32]

To investigate the cycling stability, a 10,000-cycle test at a current density of 4 A g^{-1} was carried out (Figure 4e). During the initial 482 cycles, the specific capacitance increased as the electrode was gradually activated. However, a slight decrease in

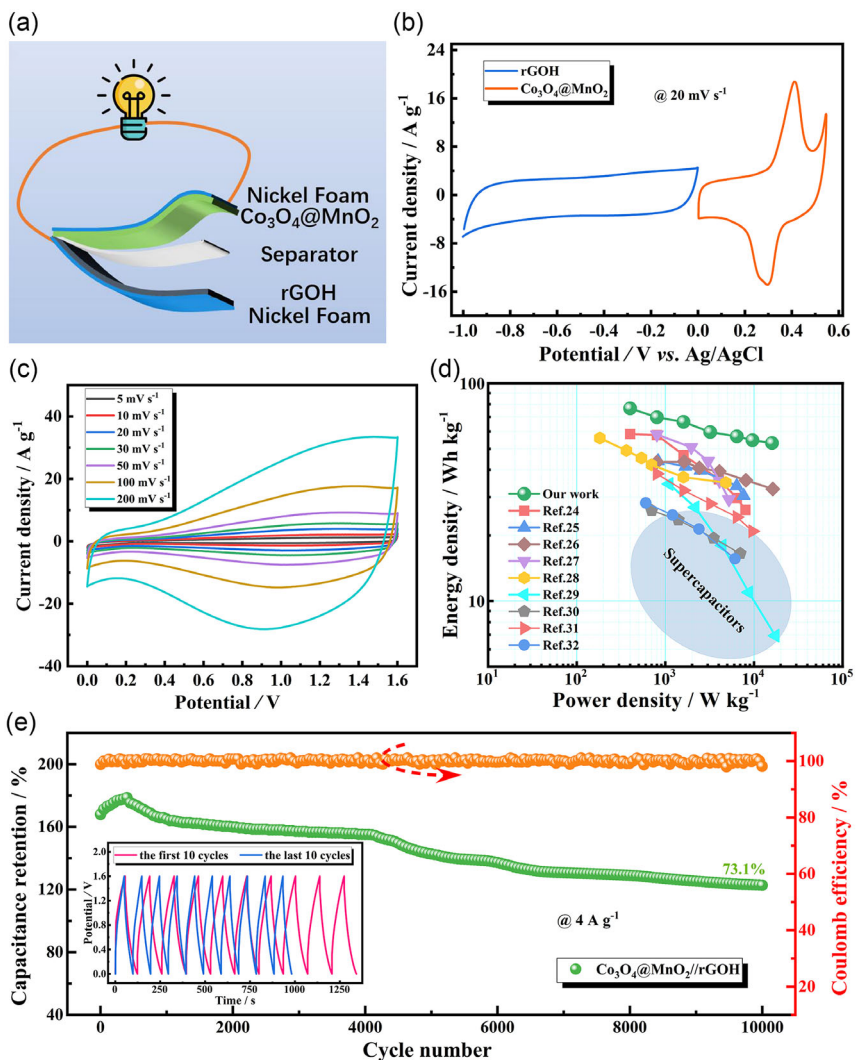


Figure 4. Electrochemical performance of $\text{Co}_3\text{O}_4@\text{MnO}_2||\text{rGOH}$: a) Device schematic. b) CV curves of rGOH and $\text{Co}_3\text{O}_4@\text{MnO}_2$ at 20 mV s^{-1} . c) CV curves at different scan rates. d) Ragone plots. e) Capacitance retention and coulombic efficiency. The inset compares GCD curves of the 1st and last 10 cycles.

Table 1. Comparison of $\text{Co}_3\text{O}_4@\text{MnO}_2||\text{rGOH}$ performance with reported works in the literature.

Materials	Capacitance	Maximum energy density	Maximum power density	Ref.
$\text{Co}_3\text{O}_4@\text{Co/NC-HN}$	164.34 F g^{-1} at 1 A g^{-1}	$58.43 \text{ W h kg}^{-1}$ at 400 W kg^{-1}	$26.22 \text{ W h kg}^{-1}$ at 8000 W kg^{-1}	[24]
$\text{Co}_3\text{O}_4@\text{C}$	127.06 F g^{-1} at 1 A g^{-1}	$43.99 \text{ W h kg}^{-1}$ at 824 W kg^{-1}	30.5 W h kg^{-1} at 7625.9 W kg^{-1}	[25]
$\text{Co}_3\text{O}_4@\text{NiCoLDH}$	125 F g^{-1} at 1 A g^{-1}	$44.44 \text{ W h kg}^{-1}$ at 800 W kg^{-1}	$32.67 \text{ W h kg}^{-1}$ at $16,000 \text{ W kg}^{-1}$	[26]
$\text{Co}_3\text{O}_4@\text{CoNi}_2\text{S}_4$ on CC	163 F g^{-1} at 1 A g^{-1}	58.1 W h kg^{-1} at 799.99 W kg^{-1}	$29.29 \text{ W h kg}^{-1}$ at 5209 W kg^{-1}	[27]
$\text{Co}_3\text{O}_4@\text{NiO}$	\	56 W h kg^{-1} at 182 W kg^{-1}	$34.95 \text{ W h kg}^{-1}$ at 4822.8 W kg^{-1}	[28]
NF/C- $\text{Co}_3\text{O}_4/\text{PPy}$	205.1 F g^{-1} at 1 A g^{-1}	$34.44 \text{ W h kg}^{-1}$ at 1100 W kg^{-1}	4.15 W h kg^{-1} at $35,204 \text{ W kg}^{-1}$	[29]
Co-MXene-2	95.75 F g^{-1} at 1 A g^{-1}	$26.06 \text{ W h kg}^{-1}$ at 700 W kg^{-1}	$16.53 \text{ W h kg}^{-1}$ at 700 W kg^{-1}	[30]
CF@ $\text{CoS}_2/\text{Co}_3\text{O}_4/\text{CNFs}$ nanosheet	\	38.4 W h kg^{-1} at 800 W kg^{-1}	20.9 W h kg^{-1} at 9600 W kg^{-1}	[31]
$\text{MnO}_2/\text{Co}_3\text{O}_4/\text{NB-PCNF}$	109.97 F g^{-1} at 0.5 A g^{-1}	28.2 W h kg^{-1} at 600 W kg^{-1}	$15.63 \text{ W h kg}^{-1}$ at 6108.3 W kg^{-1}	[32]
$\text{Co}_3\text{O}_4@\text{MnO}_2$	215.4 F g^{-1} at 0.5 A g^{-1}	78.2 W h kg^{-1} at 325 W kg^{-1}	$52.22 \text{ W h kg}^{-1}$ at $11,500 \text{ W kg}^{-1}$	Our work

capacitance was observed in subsequent cycles, likely because of the partial detachment of active materials during the cycling process. Comparison of the GCD curves before and after 10,000 cycles revealed that the device retained 73.1% of its initial capacitance, whereas the coulombic efficiency remained consistently close to 100% throughout the cycling test, confirming the excellent charge reversibility and cycling stability of the $\text{Co}_3\text{O}_4@\text{MnO}_2||\text{rGOH}$ device.

Figure 5a presents the results for $\text{Co}_3\text{O}_4@\text{MnO}_2||\text{rGOH}$ after 2000 charge-discharge cycles at five bending angles and a current density of 4 A g^{-1} . Switching between bending angles had a negligible impact on the capacitance, showing only a 7% reduction in capacitance retention compared with the flat state. Furthermore, the coulombic efficiency remained close to 100%

throughout the bending cycles, demonstrating excellent electrochemical reversibility and stability. Figure 5b compares the GCD curves of the device after 2000 cycles in each bending condition. As shown, the curves are similar, confirming device reliability. However, the observed reduction in the charge-discharge time may be attributed to the detachment of active materials caused by mechanical stress during bending. To systematically investigate the flexibility of the device, we conducted 10,000 charge-discharge cycles at different bending states (0° , 45° , 90° , 180° , and rolled). As illustrated in Figure S7, Supporting Information, the corresponding capacitance retention was 72.8%, 71.1%, 69.6%, 68.6%, and 65.2%, respectively. To enhance the working voltage or prolong the discharge time, series and parallel configurations of the devices were tested, and the

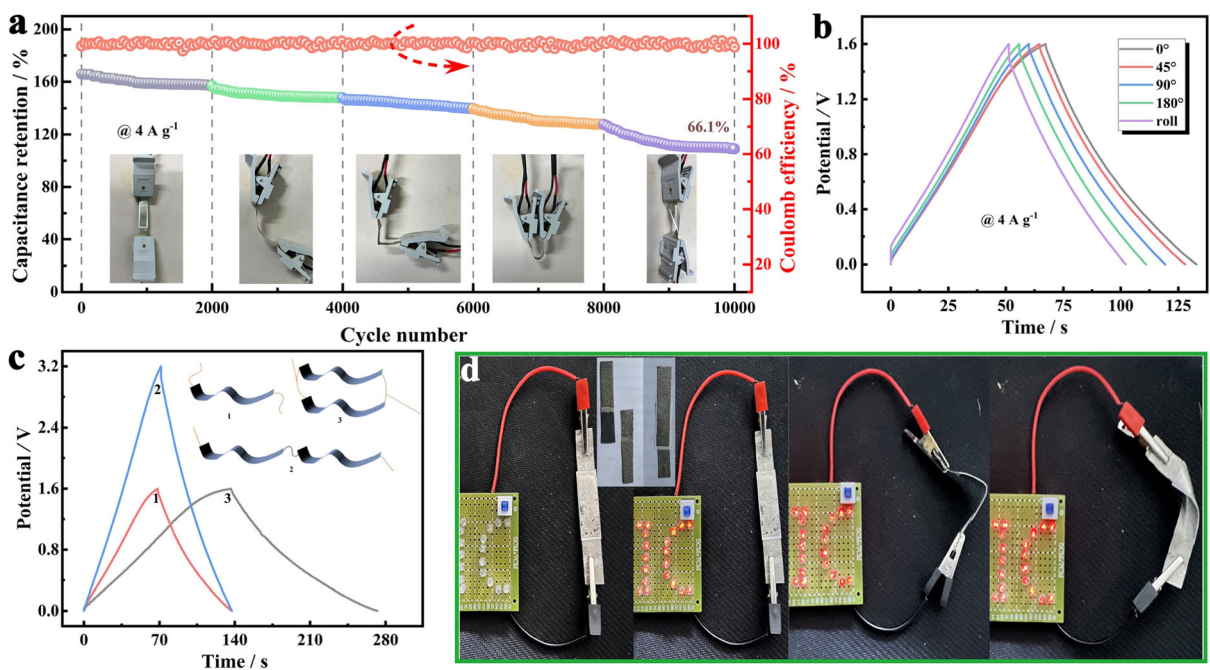


Figure 5. a) Capacitance retention and coulombic efficiency as a function of cycle number at 4 A g^{-1} under mechanical deformation (left to right: 0° , 45° , 90° , 180° , and rolled states; insets show corresponding photographs). b) GCD profiles of the device at 4 A g^{-1} under mechanical deformation over 2000 cycles. c) Representative charge-discharge curves at 4 A g^{-1} , showing stable performance. d) Sequential images of the flexible supercapacitor device powering LEDs under bending and rolling conditions.

corresponding GCD curves are shown in Figure 5c. The results revealed that compared with a single device, the series and parallel configurations successfully doubled the voltage and current, respectively, significantly improving the overall performance of the device. Notably, even after bending, the flexible device could continuously power 19 yellow light-emitting diodes (LEDs) for approximately 300 s, in both flat and rolled states (Figure 5d). These findings highlight the excellent mechanical adaptability, superior performance, and significant potential of this flexible device for practical applications under various mechanical conditions.

4. Conclusion

In summary, Co_3O_4 nanocages were synthesized using cubic $\text{Co}_3[\text{Co}(\text{CN})_6]_2$ as a precursor. Then, $\text{Co}_3\text{O}_4@\text{MnO}_2$ composites having hollow cubic core–shell structures were prepared using a hydrothermal method. The $\text{Co}_3\text{O}_4@\text{MnO}_2$ composites demonstrated remarkable electrochemical properties, achieving a specific capacitance of 670.2 F g^{-1} at a current density of 1 A g^{-1} . In addition, an all-solid-state flexible supercapacitor was assembled using $\text{Co}_3\text{O}_4@\text{MnO}_2$ as the positive electrode, rGOH as the negative electrode, and $\text{Na}_2\text{SO}_4\text{-PVA}$ as the electrolyte. The device showed impressive performance, having a maximum energy density of 78.2 W h kg^{-1} and a power density of 325 W kg^{-1} . Even at a high power density of $11,500 \text{ W kg}^{-1}$, the energy density remained at 55.2 W h kg^{-1} . Durability tests indicated that the device retained 73.1% of its initial capacitance after 10,000 charge–discharge cycles. Moreover, under five different bending conditions and after 10,000 cycles, the device retained 66.1% of its initial capacitance, demonstrating excellent mechanical stability and long-term reliability. These results provide a strong basis for advancing the design and development of next-generation high-performance energy-storage materials.

Acknowledgements

We sincerely acknowledge the financial support for this research provided by the Key Research and Development Program (Talents Introduction Project) of Ningxia (Grant No. 2021BEB04027), the Fundamental Research Funds for the Central Universities, North Minzu University (Grant No. 2021KJX04), the Natural Science Foundation of Ningxia Province (Grant No. 2022AAC05033), the Fundamental Research Funds for the Central Universities, North Minzu University (Grant No. 2020KYQD18).

Conflict of Interest

The authors declare no conflict of interest.

Author Contributions

Xu Zhang: funding acquisition (lead); resources (lead); writing—review and editing (lead). **Chuang Pang:** formal analysis (lead); writing—original draft (lead). **Keyu Zhao:** data curation (lead); investigation (lead). **Heng Xiang:** visualization (lead). **Zhongli Zou:** supervision (lead). **Kui Cheng:** methodology (lead).

Data Availability Statement

The data that support the findings of this study are available from the corresponding author upon reasonable request.

Keywords: all-solid-state • core-shell structure • flexibility • supercapacitor • transition metal oxides

- [1] a) X. Jian, H. M. Yang, J. G. Li, E. H. Zhang, L. L. Cao, Z. H. Liang, *Electrochim. Acta* **2017**, *228*, 483; b) R. Nasser, H. Zhou, H. Elhouichet, S. Melhi, Z. Li, J. M. Song, *Chem. Eng. J.* **2024**, *489*, 151554; c) Z. C. Ling, Q. He, H. B. Yang, Z. Zhou, Z. M. Han, X. H. Luo, K. P. Yang, Q. F. Guan, S. H. Yu, *Adv. Mater.* **2024**, *36*, 2402695.
- [2] a) S. Mallick, P. P. Jana, C. R. Raj, *ChemElectroChem*, **5**, *2018*, 2348; b) I. N. Reddy, B. Akkinepally, C. Bai, J. Shim, *Inorg. Chem. Commun.* **2023**, *154*, 110954.
- [3] a) S. K. Shinde, S. M. Mohite, A. A. Kadam, H. M. Yadav, G. S. Ghodake, K. Y. Rajpure, D. S. Lee, D. Y. Kim, *J. Electroanal. Chem.* **2019**, *850*, 113433; b) H. Li, A. Liu, H. Che, *Mater. Sci. Semicond. Process.* **2019**, *91*, 115.
- [4] S. K. Meher, G. R. Rao, *J. Phys. Chem. C* **2011**, *115*, 15646.
- [5] a) X. Du, C. Hou, H. Kimura, J. Song, X. Yang, X. Xie, H. Jiang, X. Zhang, X. Sun, Y. Zhang, S. Gao, W. Du, *J. Colloid Interface Sci.* **2024**, *673*, 92; b) S. A. Beknalkar, A. M. Teli, T. S. Bhat, K. K. Pawar, S. S. Patil, N. S. Harale, J. C. Shin, P. S. Patil, *J. Mater. Sci. Technol.* **2022**, *130*, 227.
- [6] S. I. Kim, J. S. Lee, H. J. Ahn, H. K. Song, J. H. Jang, *ACS Appl. Mater. Interfaces* **2013**, *5*, 1596.
- [7] M. Zhi, C. Xiang, J. Li, M. Li, N. Wu, *Nanoscale* **2013**, *5*, 72.
- [8] a) J. Jiang, A. Kucernak, *Electrochim. Acta* **2002**, *47*, 2381; b) C. Zhou, X. Wu, C. Luo, Z. Liu, L. Wang, C. Yang, H. Yu, *Sustainable Mater. Technol.* **2024**, *40*, e00891.
- [9] a) J. Mei, T. Liao, G. A. Ayoko, J. Bell, Z. Sun, *Prog. Mater Sci.* **2019**, *103*, 596; b) Y. Meng, C. Liang, D. Jiang, Y. Zhang, J. Su, X. Xu, M. Lu, *J. Energy Storage* **2023**, *74*, 109105.
- [10] G. Liu, C. Kang, J. Fang, L. Fu, H. Zhou, Q. Liu, *J. Power Sources* **2019**, *431*, 48.
- [11] K. Allado, M. Liu, A. Jayapalan, D. Arvapalli, K. Nowlin, J. Wei, *Energy Fuels* **2021**, *35*, 8396.
- [12] a) X. Zhang, J. Jiang, Y. Chen, K. Cheng, F. Yang, J. Yan, K. Zhu, K. Ye, G. Wang, L. Zhou, D. Cao, *Chem. Eng. J.* **2018**, *335*, 321; b) Y. Xie, X. Sheng, D. Xie, Z. Liu, X. Zhang, L. Zhong, *Carbon* **2016**, *109*, 673.
- [13] X. Wang, Y. Xu, L. Shao, Y. Wei, X. Zhang, X. An, J. Liu, C. Zhou, Y. Chen, G. Wang, *J. Energy Storage* **2023**, *63*, 107056.
- [14] Y. Chen, C. Kang, L. Ma, L. Fu, G. Li, Q. Hu, Q. Liu, *Chem. Eng. J.* **2021**, *417*, 129243.
- [15] a) X. Wang, C. Jing, W. Zhang, X. Wang, X. Liu, B. Dong, Y. Zhang, *Appl. Surf. Sci.* **2020**, *532*, 147437; b) L. Wan, Y. Yuan, J. Liu, J. Chen, Y. Zhang, C. Du, M. Xie, *Electrochim. Acta* **2021**, *368*, 137579.
- [16] Z. X. Wang, F. F. Tang, T. Li, X. Z. Jiang, J. T. Xu, L. Cui, J. Q. Liu, *J. Energy Storage* **2024**, *101*, 113776.
- [17] X. Huang, Y. Li, X. Yan, F. Zhang, C. Chu, J. Wu, J. Pan, Z. Shahnavaz, J. M. Moradian, *J. Materiomics* **2024**, *10*, 552.
- [18] J. Wang, Y. Huang, X. Du, S. Zhang, M. Zong, *Chem. Eng. J.* **2023**, *464*, 142741.
- [19] N. Jabeen, A. Dahshan, H. H. Hegazy, A. Hussain, N. ul Hassan, *Electrochim. Acta* **2024**, *478*, 143874.
- [20] a) Y. Ouyang, H. Ye, X. Xia, X. Jiao, G. Li, S. Mutahir, L. Wang, D. Mandler, W. Lei, Q. Hao, *J. Mater. Chem. A* **2019**, *7*, 3228; b) Y. Wang, S. Yu, C. Y. Deng, H. L. Wei, J. H. Zhou, Z. X. Chen, H. Yang, M. J. Liu,

- B. N. Gu, C. C. Chung, H. F. Lv, Z. Y. Zhou, Y. L. Chueh, *ACS Appl. Mater. Interfaces* **2022**, *14*, 8282.
- [21] a) H. Wang, K. Zhang, Y. Song, J. Qiu, J. Wu, L. Yan, *Carbon* **2019**, *146*, 420;
b) S. Liu, K. S. Hui, K. N. Hui, *ChemNanoMat* **2015**, *1*, 593.
- [22] Y. C. Ding, Y. Q. Peng, S. H. Chen, Z. Q. Li, X. X. Zhang, P. Falaras, L. H. Hu, *Appl. Surf. Sci.* **2019**, *495*, 143502.
- [23] A. Irshad, S. Zulfiqar, Z. A. Alothman, I. Shakir, M. F. Warsi, E. W. Cochran, *Fuel* **2024**, *362*, 130705.
- [24] L. Wang, X. Li, S. Xiong, H. Lin, Y. Xu, Y. Jiao, J. Chen, *J. Colloid Interface Sci.* **2021**, *600*, 58.
- [25] T. Shu, H. Wang, Q. Li, Z. P. Feng, F. X. Wei, K. X. Yao, Z. Sun, J. Q. Qi, Y. W. Sui, *Chem. Eng. J.* **2021**, *419*, 72.
- [26] X. M. Yin, H. J. Li, R. M. Yuan, J. H. Lu, *J. Mater. Sci. Technol.* **2021**, *62*, 60.
- [27] Z. Duan, X. R. Shi, C. Sun, W. Lin, S. Huang, X. Zhang, M. Huang, Z. Yang, S. Xu, *Electrochim. Acta* **2022**, *412*, 459.
- [28] N. R. Reddy, P. M. Reddy, T. K. Mandal, K. R. Reddy, N. P. Shetti, T. A. Saleh, S. W. Joo, T. M. Aminabhavi, *J. Environ. Manage.* **2021**, *298*, 178.
- [29] S. Karingula, S. K. Venishetty, Y. G. Kotagiri, K. V. Gobi, *J. Energy Storage* **2024**, *75*, 109641.
- [30] Y. M. Zhang, J. M. Cao, Z. Y. Yuan, L. J. Zhao, L. L. Wang, W. Han, *J. Colloid Interface Sci.* **2021**, *599*, 109.
- [31] C. H. Wang, Q. J. Yang, Y. Liu, L. Sun, R. M. Luo, W. D. Shi, *Colloids Surf. A* **2023**, *656*, 876.
- [32] X. L. Zhang, G. L. Yan, Z. Y. Li, J. Y. Chen, L. Wang, H. Li, Y. P. Wu, *Appl. Surf. Sci.* **2024**, *648*, 720.

Manuscript received: April 18, 2025

Revised manuscript received: August 29, 2025

Version of record online:
